

# RSC Advances



This is an *Accepted Manuscript*, which has been through the Royal Society of Chemistry peer review process and has been accepted for publication.

*Accepted Manuscripts* are published online shortly after acceptance, before technical editing, formatting and proof reading. Using this free service, authors can make their results available to the community, in citable form, before we publish the edited article. This *Accepted Manuscript* will be replaced by the edited, formatted and paginated article as soon as this is available.

You can find more information about *Accepted Manuscripts* in the [Information for Authors](#).

Please note that technical editing may introduce minor changes to the text and/or graphics, which may alter content. The journal's standard [Terms & Conditions](#) and the [Ethical guidelines](#) still apply. In no event shall the Royal Society of Chemistry be held responsible for any errors or omissions in this *Accepted Manuscript* or any consequences arising from the use of any information it contains.

# Controllable synthesis of uniform BiOF nanosheets and the improved photocatalytic activity by high-energy (002) facet exposed and internal electric field

Sijia Zou, Fei Teng\*, Chao Chang, Zailun Liu, Shurong Wang

Jiangsu Engineering and Technology Research Center of Environmental Cleaning Materials (ECM), Jiangsu Key Laboratory of Atmospheric Environment Monitoring and Pollution Control (AEMPC), Jiangsu Joint Laboratory of Atmospheric Pollution Control (APC), Collaborative Innovation Center of Atmospheric Environment and Equipment Technology (AEET), School of Environmental Science and Engineering, Nanjing University of Information Science & Technology, China

## Abstract

To date, it still remains a big challenge to develop a new photocatalyst for photocatalysis technology. Herein, the BiOF photocatalyst with a regular nanosheet shape have been, for the first time, prepared by a simple hydrothermal method. The samples are characterized by X-ray diffraction (XRD), scanning electron microscopy (SEM), high-resolution transmission electron microscopy (HRTEM), ultraviolet-visible diffuse reflectance spectrum (UV-DRS), electrochemistry impedance spectrum (EIS) and nitrogen sorption isotherms. Also, the *Ab initio* density functional theory (DFT) calculations have been carried out to give an insight into the energy

---

\* Corresponding author. Tel./Fax.: +86-25-9882-1090; Email address: tfwd@163.com

band and electronic structures of BiOF. Further, rhodamine B (RhB) is chosen as the representative dye pollutant to evaluate the photocatalytic activity of BiOF. The results show that the uniform BiOF nanosheets grow preferentially along the [110] and [100] orientation, and 75.4% of (002) facets are exposed. After 60-min ultraviolet light irradiation ( $< 420$  nm), 79.3% of RhB is degraded by BiOF, while only 33.7% of RhB is degraded by commercial rutile  $\text{TiO}_2$ . The apparent kinetic rate constant ( $0.02534 \text{ min}^{-1}$ ) over BiOF is 3.88 times as high as that ( $0.00652 \text{ min}^{-1}$ ) over rutile  $\text{TiO}_2$ . Moreover, the calculation results demonstrate that the high-energy (002) facets are more active than the low-energy (020) and (200) facets. For the layered BiOF, there is an internal electric field (IEF) perpendicular to the  $[\text{Bi}_2\text{O}_2]^{2+}$  slabs and fluorine anionic slabs, favors for the efficient separation of photogenerated electrons and holes. It is the synergetic effect of surface structure and bulk IEF that greatly improve the activity of BiOF nanosheets. We expect that bulk IEF adjustment is another new strategy to develop new, efficient photocatalyst for the layered materials.

**Keywords:** High-energy (002) facets; Internal electric field (IEF); BiOF; Nanosheets

## 1. Introduction

Since the first report by Fujishima and Honda,<sup>1</sup> photocatalytic technology has been intensively studied and various photocatalysts have been developed. Besides TiO<sub>2</sub>,<sup>2</sup> the other efficient photocatalysts have also been developed, such as oxides<sup>3</sup>, sulfides,<sup>4</sup> oxysalts,<sup>5</sup> polymers,<sup>6</sup> and so on. Recently, bismuth-based compounds, as the efficient photocatalysts, have drawn a lot of attention. Usually, bismuth-based compounds possess the hybridized band structures due to the lone pair electrons of Bi<sup>3+</sup>.<sup>7</sup> Among them, bismuth oxyhalides as a new class of photocatalysts comprises a layer of [Bi<sub>2</sub>O<sub>2</sub>] slabs interleaved by the double slabs of halogen.<sup>8</sup> Due to their unique layered structures, there is a strong internal electrostatic field (IEF) between the slabs layers, which is perpendicular to the slabs layers.<sup>9</sup> As a result, the separation of photogenerated electron and hole can be greatly improved by the IEF, and a high photocatalytic activity can be achieved for bismuth oxyhalides.<sup>9</sup> On base of the electronic structures calculated by density functional theory (DFT), BiOF has a direct band gap, whereas the other three BiOX (Cl, Br, I) materials present an indirect band gap.<sup>10</sup> To the best of our knowledge, the BiOX (Cl, Br, I) photocatalyst have been studied extensively. In particular, the crystal orientations of these three materials have been well controlled.<sup>11,12</sup> However, BiOF has been scarcely reported as a photocatalyst.<sup>13</sup> Furthermore, it is well known that the chemistry properties of fluorine are significantly different from those of Cl, Br and I. Because of the highest electronegativity of fluorine,<sup>14,15</sup> The fluorine can strongly adsorb or trap electrons, thus effectively affecting the electron distribution. It has been widely reported that the activity of photocatalyst can be effectively improved by fluorine.<sup>16-21</sup> The current question for us is that whether BiOF has the same crystal facet effect as BiOX (X= Cl,

Br, I) or not, which is needed to be investigated extensively and answered clearly. Moreover, most of researches have focused on surface properties of catalysts, it is desirable to develop catalytic materials by explore and employ new strategy. We expect that bulk IEF adjustment is another new strategy to develop new, efficient photocatalyst for the layered materials.

Herein, the uniform BiOF nanosheets are, for the first time, achieved by a simple hydrothermal method. We have mainly investigated the influence of pH on the samples, because bismuth-containing inorganic salts precursors are fairly sensitive to the pH value.<sup>22</sup> Besides, we have investigated the photocatalytic activity of BiOF for the degradation of RhB dye. Finally, we have calculated surface energies of (002), (020) and (200) facets and the electronic structure of BiOF. Moreover, we have revealed the correlation of photocatalytic properties with active facets and IEF of BiOF.

## 2. Experimental

### 2.1 Sample preparation

All reagents were of analytical grade, purchased from Beijing Chemical Reagents Industrial Company of China, and were used without further purification.

In a typical synthesis, 1 mmol  $\text{Bi}(\text{NO}_3)_3 \cdot 5\text{H}_2\text{O}$  was dissolved in 15 mL mixture of  $\text{C}_2\text{H}_5\text{OH}-\text{H}_2\text{O}$  (the volume ratio is 14:1 ) under magnetically stirring at room temperature. Then, 6 mmol  $\text{NH}_4\text{F}$  was added into the above solution under stirring. After stirring for 1 h, 15 mL of 2 mol/L  $\text{NH}_3 \cdot \text{H}_2\text{O}$  was added into the above solution. The resulting suspension was transferred into a Teflon-lined stainless steel autoclave and maintained at the 160 °C for 12 h. The resultant precipitate was washed with distilled water and absolute ethanol for several times, respectively. Finally the sample

was dried at 60 °C for 6 h.

## 2.2 Characterization

The crystal phases of the samples were characterized by X-ray diffraction (XRD, Rigaku D/max-2550VB), using graphite monochromatized Cu K $\alpha$  radiation ( $\lambda=0.154$  nm) in the range of 20–80°(2 $\theta$ ) at a scanning rate of 5°min<sup>-1</sup>. The accelerating voltage and applied current were 40 kV and 50 mA. The samples were characterized on a scanning electron microscope (SEM, Hitachi SU-1510) with an acceleration voltage of 15 keV. The samples were coated with 5-nm-thick gold layer before observations. The fine surface structures of the samples were determined by high-resolution transmission electron microscopy (HRTEM, JEOL JEM-2100F) equipped with an electron diffraction (ED) attachment with an acceleration voltage of 200 kV. UV-vis diffused reflectance spectra of the samples were obtained using a UV-vis spectrophotometer (UV-2550, Shimadzu, Japan). BaSO<sub>4</sub> was used as a reflectance standard in a UV-vis diffuse reflectance experiment. Nitrogen sorption isotherms were performed at 77 K and < 10<sup>-4</sup> bar on a Micromeritics ASAP2010 gas adsorption analyzer. Each sample was degassed at 150 °C for 5 h before measurements. Surface area and the pore size distribution were calculated by the Brunauer-Emmett-Teller (BET) methods.

## 2.3 Electrochemical impedance spectroscopy (EIS) measurement

Electrochemical impedance spectroscopy (EIS) was performed from 0.1Hz to 100 kHz at an open circuit potential of 0.3 V, and an alternating current (AC) voltage amplitude of 5 mV in 1 M KNO<sub>3</sub> aqueous solution. The data were analyzed by ZSimWin software.

## 2.4 Evaluation of photo catalytic activity

Under UV light irradiation, the photo catalytic activities of the samples were evaluated using RhB as the probing molecule. Typically, 0.1 g of BiOF was added into the dye solution (200 mL, 10 mg L<sup>-1</sup>). Under darkness, the suspension was stirred for 30 min to reach an adsorption–desorption equilibrium of dye molecules on the photo catalyst, then it was irradiated with a 500 W Xe arc lamp equipped with ultraviolet light ( $\lambda \leq 420$  nm). During photoreaction, 4 mL of suspension was collected at a given interval time and centrifuged to remove the solids. The concentration of dye was determined by using UV–vis spectrophotometer.

## 2.5 Theory calculation

All calculations were carried out using the density of functional theory (DFT) with the exchange-correlation function described by GGA-PBE.<sup>23</sup> A BiOF (1×1) cell was used and enabled by a VASP code, in which the projector augmented wave (PAW) method represented the electron-ion interaction with a kinetic energy cutoff of 500 eV after convergence calculation.<sup>24,25</sup> During optimizations, the energy and force converged to 10<sup>-4</sup> eV/atom and 10<sup>-3</sup> eV/Å, respectively. The k-points were 7×7×3, 7×7×1, 3×3×1 and 3×3×1 for the BiOF-bulk, BiOF-002 (1×1×4), BiOF-020 (1×2×4) and BiOF-200 (2×1×4) super cells, respectively. In energy, the k-points increase to 9×9×5, 9×9×3, 5×5×3 and 5×5×3 for the BiOF-bulk, BiOF-002 (1×1×2), BiOF 3-020 (1×1×2) and BiOF-200 (1×1×2) super cells, respectively. For DOS calculations, the k-points increase to 9×9×5 for the BiOF-bulk. To generate 20 k-points by Line-mode, between the each connecting specific points of the Brillouin zone for the band of energy calculations. The vacuum in all the models was kept at 12 Å. Surface energy is represented by the formulae (1) as follows.<sup>26</sup>

$$\gamma = \frac{1}{2A} [E_{\text{BiOF}}^{\text{slab}} - NE_{\text{BiOF}}^{\text{bulk}}] \quad (1)$$

where  $E^{\text{slab}}$  is the total energy of slab,  $E^{\text{bulk}}$  is the energy per unit of BiOF,  $N$  is the total number of unit BiOF contained in super cell, and  $A$  is the surface area of slab.

### 3. Results and discussion

#### 3.1 Effect of pH value on the samples

Fig.1 shows the XRD patterns of the samples obtained at different pH values while the other reaction conditions were kept unchanged. When 6 and 15 mL of  $\text{NH}_3 \cdot \text{H}_2\text{O}$  (2 mol/L) were added, the pH values of system were 8 and 9, respectively. The as-obtained samples are pure-phase BiOF. All the diffraction peaks of the sample prepared at pH=9 are in good agreement with the standard card (JCPDS: 73-1595). No impurities peaks, e.g.,  $\text{Bi}_2\text{O}_3$ ,  $\text{BiF}_3$  and Bi, can be detected, indicating the formation of phase-pure BiOF. The sharp and strong peaks indicate a good crystallinity of the sample. SEM images show that the samples prepared at pH=8 and 9 show the similar particles shape (Fig. S1, seeing Electronic Supporting Information (ESI)) When 3 mL of 1mol/L  $\text{HNO}_3$  is added (pH=2.6), the crystalline phase can not be determined accurately (Fig. 1). When 7 mL of 1mol/L  $\text{HNO}_3$  is added (pH=2.2), the sample is mainly composed of  $\text{Bi}_7\text{F}_{11}\text{O}_5$  phase, along with some of impurity phases that can not be defined (Fig. 1). Without adding  $\text{HNO}_3$  or  $\text{NH}_3 \cdot \text{H}_2\text{O}$ , the as-prepared sample is phase-pure  $\text{BiF}_3$ , with the irregular particle shape. (Fig. S2, seeing ESI)

It is obvious that pH value is crucial in the formation of phase-pure BiOF. It has been reported that alcohols can coordinate with Bi(III) to generate alkoxide complexes.<sup>22</sup> We could assume that a Bi(III)- $\text{C}_2\text{H}_5\text{OH}$  complex may form. The

alkoxides would slowly release the Bi(III) ions to form BiOF. The whole reactions involved could be described as follows.



Herein, the added  $\text{NH}_3 \cdot \text{H}_2\text{O}$  greatly contributes to the formation of  $[\text{BiO}]^+$ , promoting the hydrolysis of Bi(III) ions to form BiOF. It is interesting that  $\text{C}_2\text{H}_5\text{OH}$  can be used as the complexing agent to control the release of Bi(III), as well as the reaction solvent.

Typically, the sample prepared at  $\text{pH}=9$  is characterized by scanning electron microscopy (SEM) and transmission electron microscopy (TEM). The uniform, well-defined nanosheets are obtained (Figure 2a). Fig.2b shows that the nanosheets are  $(3-4) \mu\text{m} \times (3-4) \mu\text{m}$  large. From high-resolution transmission electron microscopy (HRTEM) (Figure 2c), two sets of lattice fringe spacings are determined to be 0.187 nm and 0.264 nm, which can be indexed to the (200) and (110) planes of BiOF nanosheets, respectively. This indicates that the nanosheets grow preferentially along [100] and [110] directions. The selected-area electron diffraction (SAED) pattern shows the sharp diffraction spots along the [001] zone axis. The clear diffraction spots can be identified as the (110), (200) and (1-10) planes of BiOF.

Moreover, from XRD patterns in Fig.1, the intensity ratio of (002)/(101) peaks of BiOF nanosheets is calculated to be 49/100, which is significantly smaller than that (96/100) of bulk phase (standard card), indicating that the growth of (002) facets may be suppressed. As reported in reference <sup>27</sup>, more oxygen atoms are positioned on the (001) facets, and glycerol molecule tends to bind on the (001) facet via  $\text{O}_{\text{surface}}-\text{H}-\text{O}-\text{C}$  interaction, which would suppress the growth of (001) facet along the

[001] direction. Our calculation result (Section 3.3 in main text) also shows that the (002) facet contains more oxygen atom, i.e. a high oxygen atom density on the (002) facets. Hence, ethanol molecules may tend to bind on the (002) facets via  $O_{\text{surface}}\text{-H-O-C}$  interaction. As a result, the growth of (002) would be suppressed along the [001] direction, and the growth rates of crystal in the [110] and [100] directions are much higher than that in the [001] direction, leading to the formation of nanosheets, as shown in Fig. 2d. On base of the analyses above, the (002) facets are mainly exposed for the BiOF nanosheets.

We have obtained the facet exposure ratio by the geometric calculation.<sup>27</sup> The calculation method has been reported by Wang et al.<sup>27</sup> As shown in Fig. 2d, the length, width and thickness of BiOF nanosheet are measured to be 4  $\mu\text{m}$ , 4  $\mu\text{m}$  and 0.6  $\mu\text{m}$ , respectively. As a result, the exposure percentage of the (002) facet is calculated to be 75.4%.

### 3.2 Photocatalytic activities of BiOF

Fig. 3a and b show the photoactivity curves and the apparent reaction kinetic curves of the samples for the RhB degradation under ultraviolet light ( $\lambda \leq 420$  nm). The blank experiment without adding photocatalyst demonstrates that after 60-min irradiation, 20% of RhB is degraded. After 60 min, 79.3% of RhB is degraded by BiOF, while only 33.7% of RhB is degraded by commercial rutile  $\text{TiO}_2$ . In addition, after 40 min, 79.5% of RhB is degraded by commercial P25. The apparent rate constant of commercial P25, BiOF, rutile  $\text{TiO}_2$  is  $0.04196 \text{ min}^{-1}$ ,  $0.0253 \text{ min}^{-1}$  and  $0.065 \text{ min}^{-1}$ , separately. It is obvious that the BiOF sample exhibits a higher photo catalytic activity than rutile  $\text{TiO}_2$ , but exhibits a lower photo catalytic activity than commercial P25. And the BET area of BiOF is  $2.1 \text{ m}^2 \text{ g}^{-1}$ , which is only 4.2% of that ( $50.0 \text{ m}^2 \text{ g}^{-1}$ )

of rutile  $\text{TiO}_2$ . Compared with rutile  $\text{TiO}_2$ , a higher activity of BiOF nanosheets may be decided by the other factors, instead of BET area. Herein, we mainly considered the role of internal electric field (IEF) of BiOF with a typical layer structure. As reported in references [29], IEF plays a key role in improving activity for layered BiOX photocatalysts. Fig. 3c presents the cycle experiments of BiOF for RhB degradation. The photocatalytic activity of BiOF does not decrease obviously after three cycles, indicating a good stability of BiOF.

To understand the high activity of BiOF, the electrochemical impedance spectroscopy (EIS) has been measured to investigate the electron transfer ability (Fig.3d). It is well known that a smaller semicircle radius in a Nyquist plot means a smaller electrical resistance of electrode.<sup>28</sup> The semicircle radius of rutile  $\text{TiO}_2$  is larger than that of BiOF, indicating a smaller electrical resistance of BiOF. It seems that the featured layer structure of BiOF favors for the transfer and separation of electron-hole pairs, leading to an improved photocatalytic properties.

For the BiOF layered structure, there are the strong covalent bonds in the  $[\text{Bi}_2\text{O}_2]$  intralayer and the weak interlayer van der Waals in the interlayer. As a result, the non-uniform charge distribution will polarize the relative atoms and atomic orbitals to induce an internal electric field (IEF).<sup>29</sup> Fig.5 shows a schematic diagram of IEF, which is perpendicular to the  $[\text{BiO}]^+$  slabs and  $\text{F}^-$  anion slabs, namely, along [001] direction. This IEF could facilitate the separation and transfer of photogenerated charges. In the other words, the unique layered structure of BiOF could be responsible for the formation of IEF. Summarily, we hold that the photocatalytic activity of BiOF can be significantly improved by IEF of BiOF, instead of BET area.

Moreover, the inset of Fig.6a shows the ultraviolet-visible diffusion reflectance spectra (UV-DRS) of BiOF. The absorption edge of BiOF occurs at 384 nm and the

band gap is determined to be 3.93 eV (Fig. 6a). It is obvious that BiOF has a wider band gap than that of rutile TiO<sub>2</sub> and Degussa P25 TiO<sub>2</sub> (Fig. 6a). For BiOX, the valance band maximum is mainly comprised of O<sub>2p</sub> and X<sub>np</sub> states (i.e.  $n=2, 3, 4$  and  $5$  for X=F, Cl, Br and I, respectively); while the conduction band minimum is mainly composed of the Bi 6p states.<sup>22</sup> It has been reported that with the increase of atomic number of X, the contribution of X<sub>np</sub> states of halogen atom ( $n=2, 3, 4$  and  $5$  for X=F, Cl, Br and I, respectively) increases remarkably, and the dispersive characteristic of energy band becomes more obvious, thus narrowing the band gap.<sup>22</sup> It is a fact that the band gaps of BiOF, BiOCl, BiOBr and BiOI are 3.93, 3.4, 2.8 and 1.8 eV, respectively.<sup>22</sup> Among them, BiOF has the widest band gap.

As observed from Fig. 6b, the absorption edge of BiOF, rutile TiO<sub>2</sub> and Degussa P25 TiO<sub>2</sub> are about 384 nm, 400 nm and 420 nm, indicating that three catalysts can be excited by ultraviolet light ( $\lambda \leq 420$  nm). And, we get the conclusion that the absorbance order are rutile TiO<sub>2</sub> > Degussa P25 TiO<sub>2</sub> > BiOF by calculating the integral area of curve. It is obvious that BiOF exhibits a lower absorbance than rutile TiO<sub>2</sub>. However, BiOF exhibits higher photo catalytic activity than rutile TiO<sub>2</sub>. We assume the result may be not decided by absorbance. Further, our calculation results (in Section 3.3) also demonstrate that the (002) facet exposed is high-energy facets which play a crucial role in improving activity of catalyst. On the other hand, due to Degussa P25 TiO<sub>2</sub> has wider absorbance edge than BiOF, Degussa P25 TiO<sub>2</sub> exhibits higher photo catalytic activity than BiOF.

Furthermore, the trapping experiments have been performed to explore the photocatalytic degradation process, in which ammonium oxalate and dimethylsulfoxide (DMSO) are used as the holes and radicals scavengers, respectively (Fig.4a). When adding 10 mL DMSO, the activity of BiOF decreases slightly, while

the degradation reaction is obviously inhibited when adding 1 mmol ammonium oxalate. This indicates that the holes could be the major oxidative species for RhB over BiOF.

### 3.3 Theory calculation

We have calculated the surface energies of the typical (002), (020) and (200) facets by using VASP package. The surface energies of (002), (020) and (200) facets are calculated to be 3.11, 1.02 and 1.02  $\text{JM}^{-2}$  (Table 1). It has been demonstrated that the high-energy facets exposed play a crucial role in improving activity of catalyst.<sup>30-32</sup> Thus the high-energy (002) facets are expected to be more active than the others.<sup>28</sup> Further observed from Figure 7 (b-d), the numbers of oxygen are determined 8, 4 and 4 on (002), (200) and (020) facets, respectively. We could expect that more oxygen atoms on the (002) facets exposed can catch the photogenerated electrons, which favors for the charge separation. As a result, the high-percentage (002) facets are beneficial to improve the activity of BiOF.

Moreover, the *Ab initio* density functional theory (DFT) calculations have been carried out to insight the energy band and electronic structures of BiOF, because electronic structure can provide an important insight into the physicochemical behavior of materials. Fig. 8 shows the energy band and electronic densities of states (DOS) of BiOF, which are calculated by the CASTEP package. In Fig. 8a, the valence band maximum (VBM) and conduction band minimum (CBM) between Z and R points confirm the direct band gap property of BiOF, in good agreement with the result of the measured absorption spectrum in Fig. 6a. The direct band gap between VBM and CBM is calculated to be 3.40 eV, with an expected diminution that is a common feature for DFT calculations<sup>33</sup>. For Bi-based semiconductors, it is usually

found that the Bi 6s and O 2p orbitals could form a preferable hybridized valence band (VB).<sup>34</sup> Furthermore, both total density of states (DOS) and the partial DOS are employed to understand the electronic properties of BiOF. In Fig.8b, the VB apex of BiOF is found to not only composed of F 2p, O 2P and Bi 6p orbitals, but also a little of Bi 6s orbitals. In addition, the CB bottom is mainly composed of the O 2p and Bi 6p orbitals. For BiOF, the charge transfer upon being photoexcited occurs from the hybrid orbits of both F 2p and O 2p to the hybrid orbits of both O 2p and Bi 6p. Summarily, the hybridized orbits favor for the separation efficiency of electrons and holes.<sup>18,19</sup> As we know, most of researchers have focused on surface properties of catalysts in recent a few years, it is desirable to develop catalytic materials by explore and employ new strategy. We expect that bulk IEF adjustment is another new strategy to develop new, efficient photocatalyst for the layered materials.

#### 4. Conclusions

To conclude, we have developed an innovative method to acquire the uniform BiOF nanosheets, of which 75.4% of high-energy (002) facets are exposed. The BiOF nanosheets show a higher activity than commercial rutile TiO<sub>2</sub>, which has mainly the synergetic effect of high-energy (002) facets exposed and bulk IEF. This study may provide us that bulk IEF adjustment is a new strategy to develop new, efficient photocatalyst for layered materials.

#### Acknowledgments

This work is financially supported by National Science Foundation of China (21377060, 20943004), the Project Funded by the Science and Technology Infrastructure Program of Jiangsu (BM201380277), Jiangsu Science Foundation of

China (BK2012862), Six Talent Climax Foundation of Jiangsu (20100292), Jiangsu Province of Academic Scientific Research Industrialization Projects (JHB2012-10.), the Key Project of Environmental Protection Program of Jiangsu (2013005), A Project Funded by the Priority Academic Program Development of Jiangsu Higher Education Institutions (PAPD) and Jiangsu Province Innovation Platform for Superiority Subject of Environmental Science and Engineering sponsored by SRF for ROCS, SEM (2013S002) and “333” Outstanding Youth Scientist Foundation of Jiangsu (2011-2015).

## References

- 1 A. Fujishima and K. Honda, *Nature*, 1972, 37-38.
- 2 R. Asahi, T. Morikawa, T. Ohwaki, K. Aoki and Y. Taga, *Science*, 2001, **293**, 269-271.
- 3 M. Muruganandham, R. Amutha, G.-J. Lee, S.-H. Hsieh, J. J. Wu and M. Sillanpää, *J. Phys. Chem. C*, 2012, **116**, 12906-12915.
- 4 L. Huang, X. Wang, J. Yang, G. Liu, J. Han and C. Li, *J. Phys. Chem. C*, 2013, **117**, 11584-11591.
- 5 S. Li, S. Liu, S. Liu, Y. Liu, Q. Tang, Z. Shi, S. Ouyang and J. Ye, *J. Am. Chem. Soc.*, 2012, **134**, 19716-19721.
- 7 T. Wen, D.-X. Zhang and J. Zhang, *Inorg. Chem.*, 2012, **52**, 12-14.
- 8 H. Huang, Y. He, Z. Lin, L. Kang and Y. Zhang, *J. Phys. Chem. C*, 2013, **117**, 22986-22994.
- 9 L. Zhang, W. Wang, J. Yang, Z. Chen, W. Zhang, L. Zhou and S. Liu, *Appl. Catal. A: Gen.*, 2006, **308**, 105-110.
- 10 X. Xiao, R. Hao, X. Zuo, J. Nan, L. Li and W. Zhang, *Chem. Eng. J.*, 2012, **209**,

- 293-300.
- 11 Y. Xu and M. A. Schoonen, *Am. Mineral.*, 2000, **85**, 543-556.
  - 12 N. Li, X. Hua, K. Wang, Y. Jin, J. Xu, M. Chen and F. Teng, *J. Mol. Catal. A*, 2014, **395**(12), 428-433.
  - 13 N. Li, X. Hua, K. Wang, Y. Jin, J. Xu, M. Chen and F. Teng, *Dalton Trans.*, 2014, **43**, 13742-13750.
  - 14 W. Su, J. Wang, Y. Huang, W. Wang, L. Wu, X. Wang and P. Liu, *Scripta Mater.*, 2010, **62**, 345-348.
  - 15 S. Liu, J. Yu, B. Cheng and M. Jaroniec, *Adv. Colloid Interface Sci.*, 2012, **173**, 35-53.
  - 16 J. C. Yu, W. Ho, J. Yu, S. Hark and K. Iu, *Langmuir*, 2003, **19**, 3889-3896.
  - 17 H. Park and W. Choi, *J. Phys. Chem. B*, 2004, **108**, 4086-4093.
  - 18 J. C. Yu, J. Yu, W. Ho, Z. Jiang and L. Zhang, *Chem. Mater.*, 2002, **14**, 3808-3816.
  - 19 D. Li, H. Haneda, N. K. Labhsetwar, S. Hishita and N. Ohashi, *Chem. Phys. Lett.*, 2005, **401**, 579-584.
  - 20 Q. Xiang, K. Lv and J. Yu, *Appl. Catal. B-Environ.*, 2010, **96**, 557-564.
  - 21 K. Lv, B. Cheng, J. Yu and G. Liu, *Phys. Chem. Chem. Phys.*, 2012, **14**, 5349-5362.
  - 22 J. Yu, Q. Li, S. Liu and M. Jaroniec, *Chem. Eur. J.*, 2013, **19**, 2433-2441.
  - 23 J. Li, Y. Yu and L. Zhang, *Nanoscale*, 2014, **6**, 8473-8488.
  - 24 J. P. Perdew, K. Burke and M. Ernzerhof, *Phys. Rev. Lett.*, 1996, **77**, 3865.
  - 25 G. Kresse and J. Furthmüller, *Phys. Rev. B*, 1996, **54**, 11169.
  - 26 G. Kresse and D. Joubert, *Phys. Rev. B*, 1999, **59**, 1758.
  - 27 D. Wang, G. Gao and Y. Zhang, *Nanoscale*, 2012, **4**, 7780.

- 28 Q. Li and X. Hu, *Phys. Rev. B*, 2006, **74**, 035414.
- 29 Y. Lv, Y. Liu, Y. Zhu and Y. Zhu, *J. Mater. Chem. A*, 2014, **2**, 1174-1182.
- 30 J. Jiang, K. Zhao, X. Xiao and L. Zhang, *J. Am. Chem. Soc.*, 2012, **134**, 4473-4476.
- 31 B. S. Naidu, B. Vishwanadh, V. Sudarsan and R. K. Vatsa, *Dalton T.*, 2012, **41**, 3194-3203.
- 32 J. Wang, F. Teng, M. Chen, J. Xu, Y. Song and X. Zhou, *Cryst. Eng. Comm.*, 2012, **15**, 39-42.
- 33 J. Shen, J. Zai, Y. Yuan and X. Qian, *Int. J. Hydrogen Energ.*, 2012, **37**, 16986-16993.
- 34 A. Kudo, H. Kato and S. Nakagawa, *J. Phys. Chem. B*, 2000, **104**, 571-575.

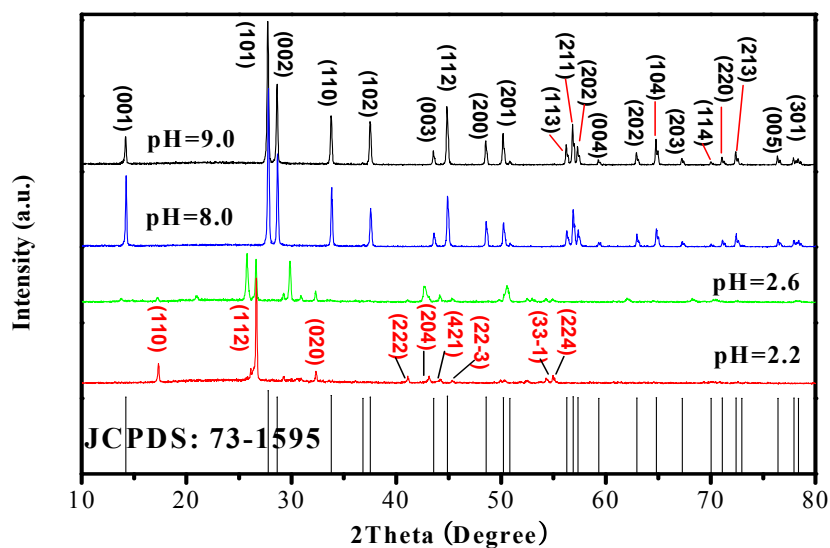


**Fig. 1** X-ray diffraction patterns (XRD) of the samples prepared at different pH values:

BiOF: JCPDS: 73-1595;  $\text{Bi}_7\text{F}_{11}\text{O}_5$ : marked with red facets indexes

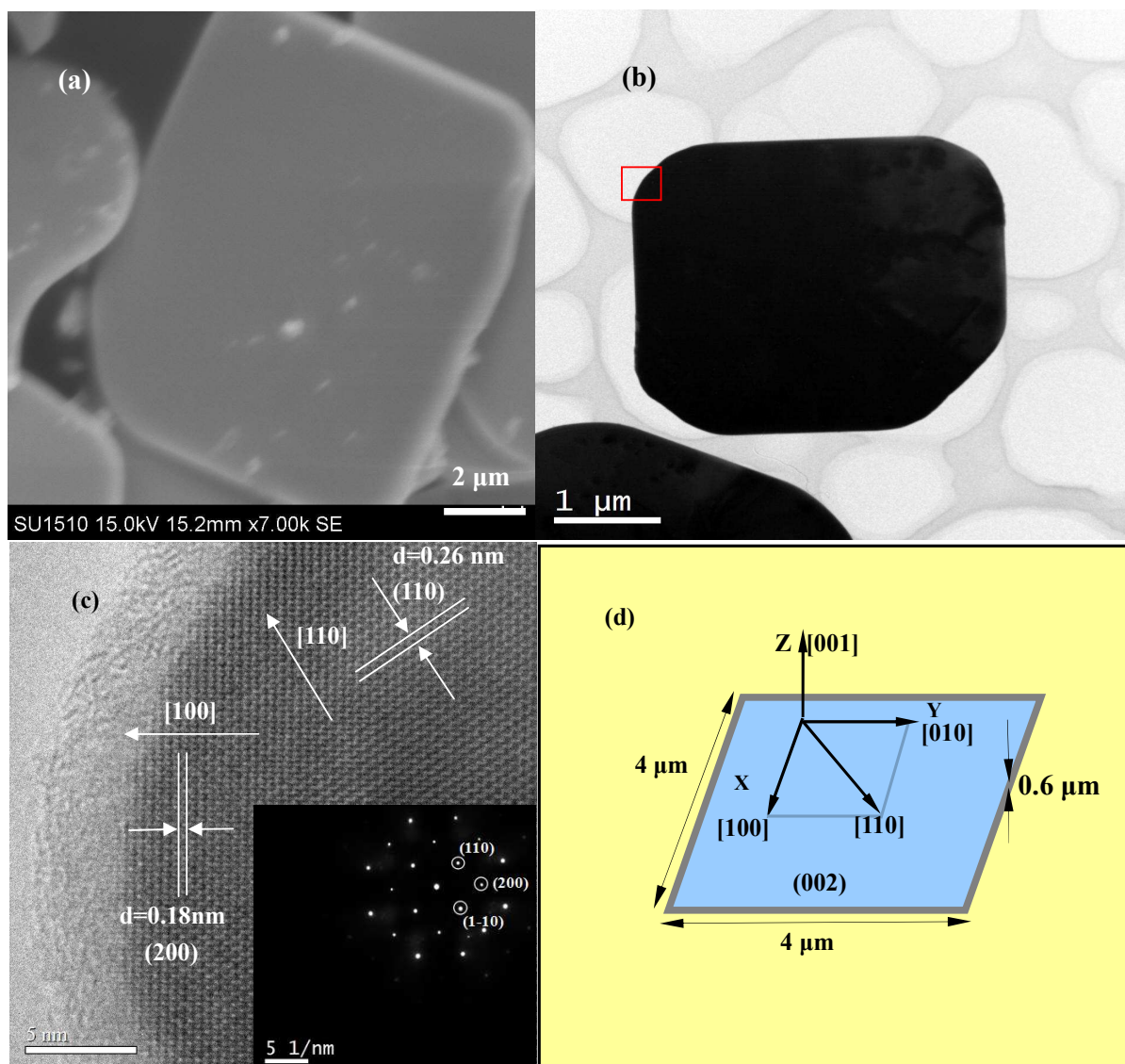


**Fig. 2** (a) SEM, (b) HRTEM images, (c) Lattice fringe image (the inset of ED patterns) of the BiOF nanosheets prepared at pH=9 and (d) calculation geometric model of a single nanosheet

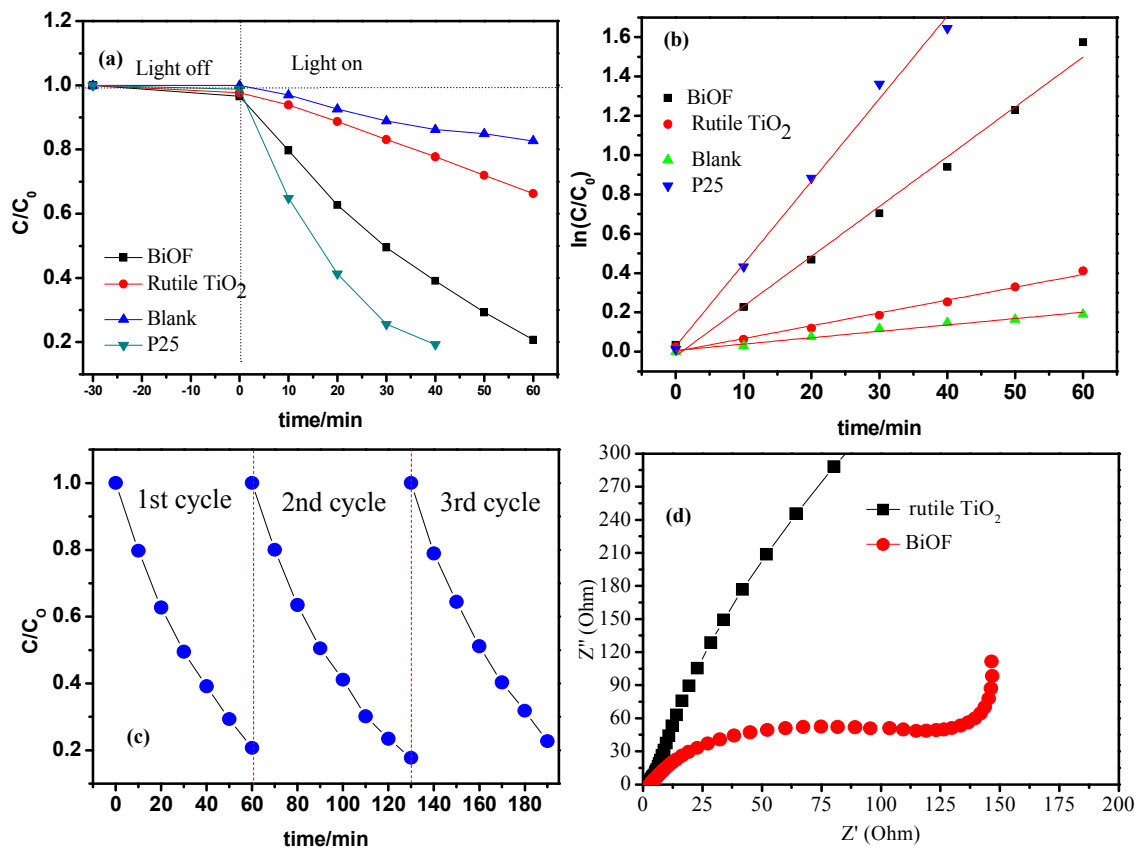


**Fig. 3** (a) Degradation curves and (b) reaction kinetic curves of RhB over the samples under UV-light irradiation ( $\lambda < 420$  nm): 200 mL of 50 mg mL<sup>-1</sup> RhB; 100 mg of powders; (c) Cycle curves; (d) Nyquist plots of electrodes in the frequency range of 0.1-10 kHz at an open circuit potential of 0.30 V in 1 M KNO<sub>3</sub> aqueous solution

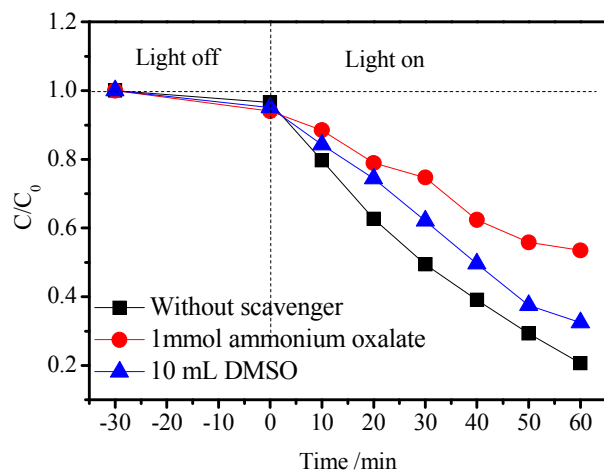


**Fig. 4** Effect of scavenger on the degradation activity of RhB over BiOF

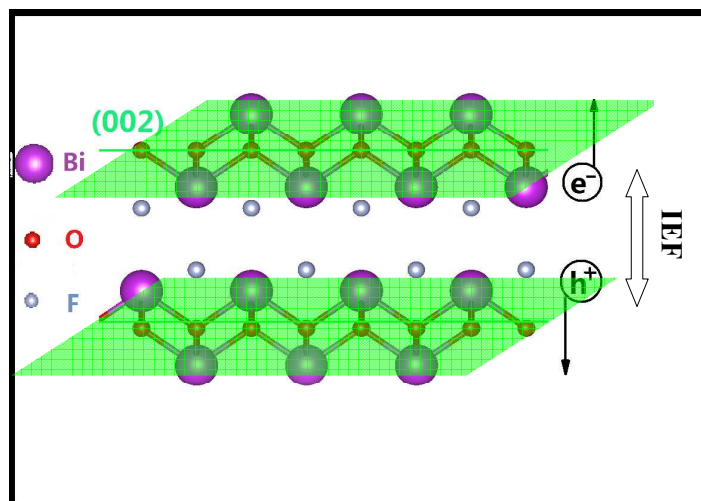


**Fig. 5** Diagram of internal electric field (IEF) within BiOF

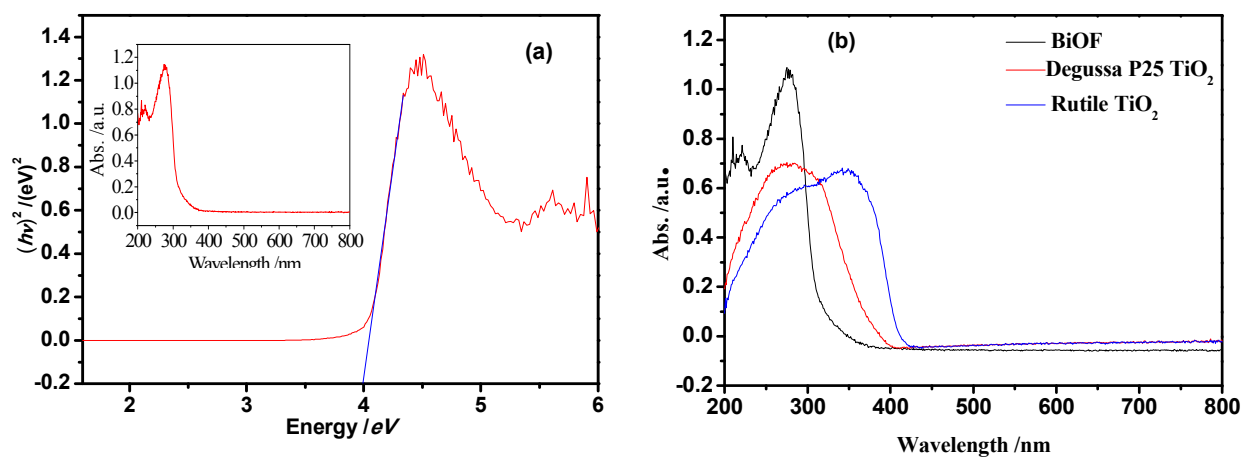


**Fig. 6** (a) Tauc plot (absorption<sup>2</sup> vs. energy) of BiOF: the inset of UV–visible diffuse reflectance spectra (UV-DRS), (b) the ultraviolet-visible diffusion reflectance spectra (UV-DRS) of BiOF, rutile  $\text{TiO}_2$  and Degussa P25  $\text{TiO}_2$

**Table 1** Surface energies of different facets of BiOF calculated by VASP package

Model	Atomic layers	Total energy (eV)	Surface energy (J/m <sup>2</sup> )
Bulk	1	-32.527217	/
002	2	-59.596692	3.11421906
020	4	-124.651986	1.020443973
200	4	-124.651986	1.020443973

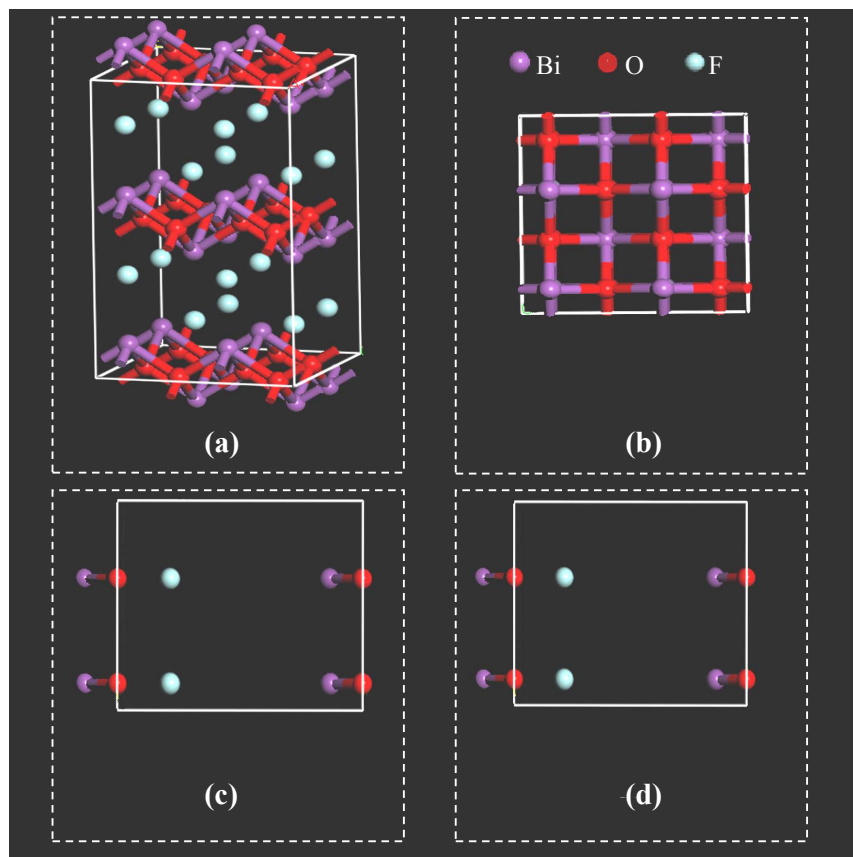


**Fig. 7** Atomic configurations of monoclinic BiOF by VASP: (a) Super cell; (b) (002); (c) (200); (d) (020)

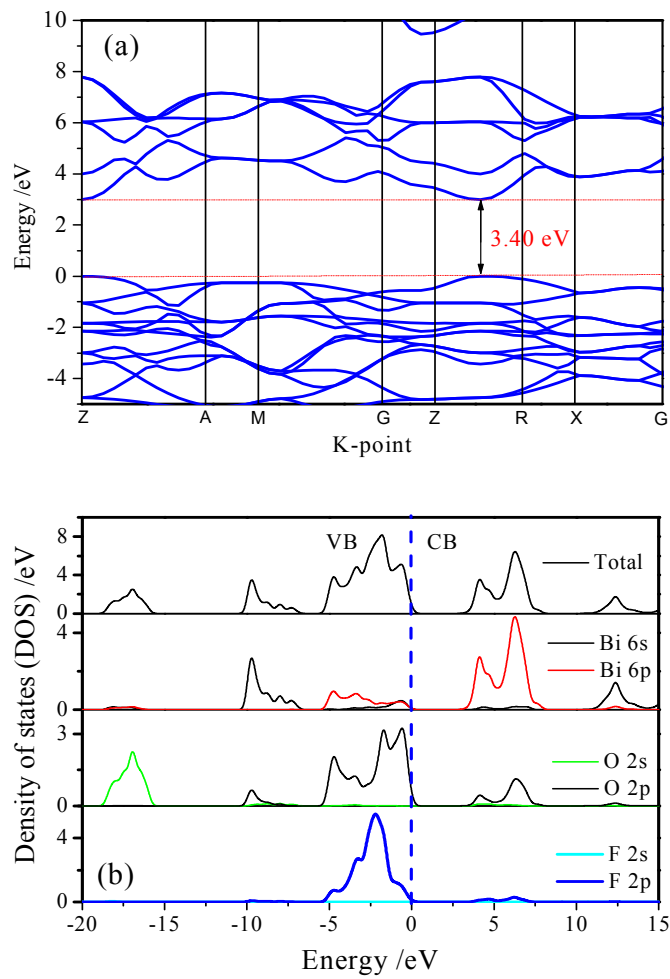


**Fig. 8** Energy bands structure (a), Total and partial density of states (DOS) (b) of BiOF